Three-Dimensional Modeling of Neutron-Based Diagnostics to Infer Plasma Conditions in Cryogenic Inertial Confinement Fusion Implosions

Introduction

In direct-drive cryogenic inertial confinement fusion (ICF)[1] implosions, a target comprising a shell of cryogenic deuterium–tritium (DT) fuel enclosing a vapor region is irradiated using multiple nearly identical laser beams. As the kinetic energy of the imploding shell is converted to the thermal energy of the hot spot, the shell undergoes deceleration and conditions relevant for achieving fusion reactions are obtained. Conditions achieved in the compressed core, at the time of peak fusion neutron production, from a typical cryogenic direct-drive implosion on the OMEGA Laser System[2] are shown in Fig. 150.54. The profile was obtained from a spherically symmetric simulation using the code *LILAC*;[3] nonuniformity was ignored in this calculation. Ideally, a hot core is surrounded by a high-density shell, although multidimensional simulations indicate that while this is largely true, the neutron-producing region is typically not centered and the high-density shell can be significantly perturbed. Perturbations are typically quantified in terms of spherical harmonics (from 3-D simulations) or Legendre modes (in 2-D experimental images or 2-D simulations).
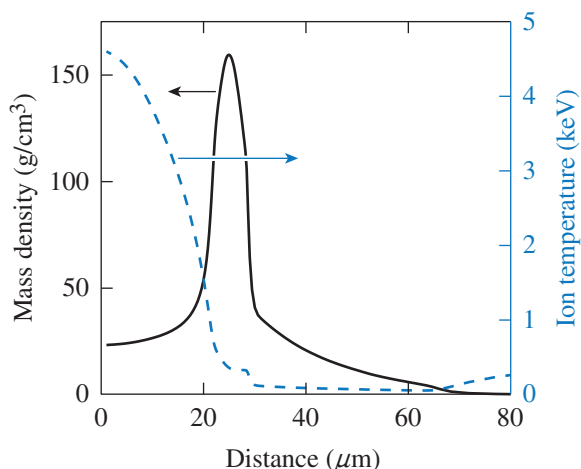

TC13274JR

Figure 150.54
A typical density and temperature profile at peak neutron production in an OMEGA cryogenic implosion.

The goal of cryogenic implosions on OMEGA is to understand the physics of directly driven ICF implosions. This requires observations that could potentially shed light on failure mechanisms including the role of long-wavelength asymmetries on target performance. Three-dimensional (3-D) direct-drive simulations that include the effect of long-wavelength asymmetries performed with the arbitrary Lagrangian–Eulerian (ALE) code *HYDRA*[4] indicate that significant long-wavelength asymmetries corresponding to spherical harmonics up to 4 should be present during the time of neutron production. These asymmetries can be seeded by power imbalance among the 60 beams of OMEGA; by beam mistiming, beam mispointing, or nonuniformities on the inside of the cryogenic layer at the ice–vapor interface; or by the initial error in the placement of the target relative to the center of the target chamber, etc. Long-wavelength asymmetries can compromise performance by reducing the clean volume over which neutrons are produced. In Fig. 150.54, the clean volume has a radius of ~20 μm. The Rayleigh–Taylor[5] growth of the nonuniformities during the deceleration phase of the imploding capsule results in growth at approximately this radius; spikes of the high-density shell penetrate the hot spot, whereas bubbles of lower-density material distort the high-density shell. These large bubbles in the high-density shell may permit heat and fuel to escape, thereby decreasing fusion yields. These asymmetries result in angular variations in areal density, defined as

$$\rho R = \int_0^R \rho(r)\mathrm{d}r,$$

the radial integral of the areal density, where $\rho(r)$ is the density along the radius of the target, and R is the outer radius of the target. Another manifestation of these asymmetries is large-scale fluid flow resulting in residual kinetic energy, i.e., kinetic energy that has not been converted to hot-spot energy. Diagnosing these asymmetries is important for identifying a potential source of performance degradation. Until recently, x-ray images from a single view have been used to infer the existence of asymmetries in OMEGA cryogenic implosions,[6,7]

although quantitative measures are outstanding. Multiple views of neutron-based diagnostics have also been available, although a tool to interpret the results has been unavailable. In this work, we show that with additional views of the neutron-based diagnostics, asymmetries can potentially be diagnosed on OMEGA. Results from a newly developed postprocessor *IRIS3D* (see **Appendix**, p. 110) for 3-D hydrodynamic codes are described here. The role of background in interpreting the various regions of the neutron spectra for the inference of areal density and its asymmetries is emphasized; the use of multiple detectors to infer a map of asymmetries is studied; and, finally, the detection of asymmetries through the effect of the residual fluid flow on neutron spectra is studied. This work is the first such analysis; future work will include detailed post-processing of 3-D simulations to compare quantities derived from neutron spectra with experiment.

The generalized Lawson criterion for ICF implosions[8] provides a measure of target performance and can be written for OMEGA scale as

$$\chi_{1\text{-D}} \approx \langle \rho R \rangle \left(\text{g/cm}^2 \right) \left[\frac{\langle T \rangle (\text{keV})}{4.4} \right]^{0.8}, \tag{1}$$

where $\langle \rho R \rangle$ is the neutron-weighted areal density of the compressed target and $\langle T \rangle$ is the neutron-weighted ion temperature in the hot spot. A value of $\chi_{1\text{-D}} \sim 1$ indicates marginal ignition, where the ratio of the output fusion neutron energy to the input laser energy is ~1. This form of the generalized Lawson criterion is derived from a power law fit to a series of spherically symmetric simulations and is written in terms of quantities—neutron-weighted areal density and ion temperature—that are, in principle, observable. As discussed later, areal density is inferred from the elastically scattered neutron spectrum,[9–11] and ion temperature is inferred from the width of the neutron spectrum of the D–T fusion neutrons.[12] Asymmetrically driven implosion experiments limit, however, the ability to directly compare the experimentally inferred quantities with spherically symmetric simulations. Areal densities can vary around the imploding target and the inferred value depends on the viewing direction. Similarly, fluid flow in the hot spot can change the width of the neutron spectrum, resulting in direction-dependent influences on the apparent ion temperature. Therefore, multiple measurements are required to constrain the values attained in implosion experiments. In addition, background neutron-producing reactions in the target can introduce ambiguities in the interpretation of neutron spectra. Therefore, it is important to understand the role of backgrounds and perform studies on different patterns of asymmetry to be able to interpret observations. Simultaneously, comparing results from 3-D hydrodynamic simulations to observations is necessary to identify the adequacy of the modeling and infer the role of nonuniformity seeds in experiments. This requires a tool to post-process 3-D simulations and compare observables with experiment.

In this article, a Monte Carlo neutron-tracking code *IRIS3D* (see **Appendix**, p. 110) is used to model neutron transport from three primary fusion reactions in a DT capsule: the 14.1-MeV D–T fusion neutrons, the 2.45-MeV D–D fusion neutrons, and the T–T three-body reaction, which results in a continuum of neutrons. Additionally, three secondary interactions of the primary D–D and D–T neutrons including the elastic scattering off the deuterium and tritium ions (used to diagnose areal density) and the neutron-induced deuteron breakup reaction (which provides a background to the elastic scattering reactions) are also modeled. Neutron-induced triton breakup is not included in this work because its cross section is ~4× smaller than the deuteron breakup reaction.[13]

In the following sections, the basic well-known relationship between ρR and elastic scattering is described;[9–11,14] the effect of neutrons from other fusion processes in the compressed target on the inference of areal density, i.e., the role of backgrounds, is discussed; and the kinematics of the elastic scattering reaction to infer the areal density in different parts of the target is exploited. The inference of areal-density asymmetries with multiple detectors is discussed along with inferring ion temperatures from neutron spectral widths. It is shown that the effect of fluid flow is an increase in the width of the neutron spectrum, leading to an increase in the inferred ion temperature. Therefore, significantly different values of ion temperature inferred from different directions around a compressing core should indicate the presence of asymmetries. It is also shown that while the absolute values of the inferred temperatures might be inaccurate, the relative values still potentially track the underlying asymmetry. Finally, conclusions are presented.

Areal Density and Elastic Scattering

The number of neutrons that scatter elastically, y'_n, as a number of primary neutrons, y_n, that move along a path s is given by

$$y'_n = \int_s y_n n \sigma \, \mathrm{d}s, \tag{2}$$

where n is the number density of deuterons or tritons (particles per unit volume) and σ is the cross section of the scattering

interaction. For the D–T primary neutrons at 14.1 MeV, the cross section for scattering off deuterons is $\sigma = \sigma_d \approx 640$ mb, and for scattering off the background tritons is $\sigma = \sigma_t \approx 930$ mb. If the substitution

$$n = \frac{\rho}{m} f \qquad (3)$$

is used, where $\overline{m}$ represents the average mass of particles in the material and f represents the fraction of particles that are of the type of interest (for DT fuel with equal proportions of D and T, $M = 2.5$ amu, and $f = 1/2$), Eq. (3) can be rewritten as

$$y'_n = \int_s y_n \frac{\rho}{m} f \sigma ds. \qquad (4)$$

The primary neutron yield y_n is not a constant along the path length since some fraction undergoes various reactions in the compressed target, including the process of elastic scattering; however, y_n typically changes by less than 10% along a path. For the purpose of illustrating the dependencies, it is assumed to be constant. The code used here takes into account the reduction of y_n along a path. Therefore, since σ and f are constants along the path length of the neutrons, the ratio of the scattered to primary neutrons can be written as (also called the down-scatter ratio or DSR)

$$\frac{y'_n}{y_n} \approx \sigma f \int_s \rho(s) ds. \qquad (5)$$

Including scattering off both the deuterons and tritons, one can write an expression for the total DSR as

$$\text{DSR} \equiv \frac{y'_n}{y_n} \approx \frac{f_d \sigma_d + f_t \sigma_t}{m} \cdot \rho L, \qquad (6)$$

where

$$\rho L = \int_0^L \rho ds$$

is the areal density along a total path length L. The DSR is the observed quantity in the experiment used to infer areal density. If the trajectories of the neutrons were purely radial, ρL would correspond to ρR, where R is the radius of the plasma. Since fusion reactions occur throughout the hot core, neutron trajec-

tories are not radial, even for spherically symmetric implosions. Therefore, comparisons between the calculated and the observed DSR are required to identify if the simulated areal density has been achieved in implosion experiments. In addition, ρL is dominantly sampled when the neutron-production rate is the highest in the experiment. Consequently, the areal density inferred in the experiment corresponds to a neutron-weighted value. In the remainder of this article, ρL and ρR will be used interchangeably. It should be kept in mind, however, that the inference of an areal density from a neutron spectrum results in a value for ρL, whereas lineouts from the center of a simulated profile would provide a measure for ρR.

To test and illustrate the physics associated with neutron interaction and transport, an ice-block profile that approximates typical profiles in a cryogenic implosion was used (Fig. 150.55). This ice-block model is characterized by regions of constant density and temperature. Neutron spectra (Fig. 150.56) using a Monte Carlo approach were calculated for the profile. Calculated cross sections for elastic scattering,[15] which previously have shown excellent agreement with measurements,[15] were used in this calculation. This Monte Carlo code, which post-processes spherically symmetric simulations, has also been compared previously with experiment and shown to be in excellent agreement when detailed capsule simulations are post-processed to obtain spectra for a limited class of implosions.[16] Of note in the neutron spectrum are the DT primary peak at 14.1 MeV and the deuteron and triton backscattered edges at 1.5 and 3.5 MeV, respectively.

The DSR is influenced by the continuous portion of the spectra as shown in Fig. 150.56. Parts of the spectra are measured in OMEGA experiments by two methods: (1) the magnetic recoil
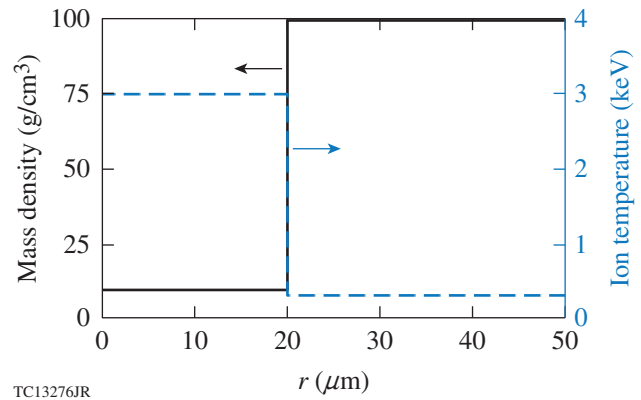

TC13276JR

Figure 150.55
A spherically symmetric "ice-block" test profile. A 50–50 DT fuel ratio was used.
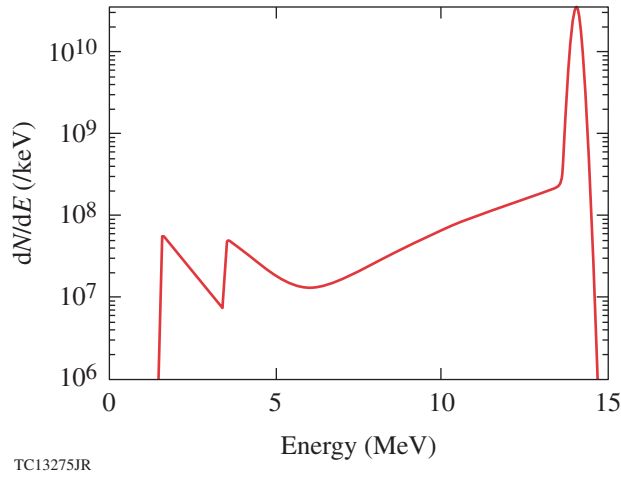
TC13275JR

Figure 150.56

Example of a neutron spectrum including only DT primary neutrons and deuteron and triton elastic scattering.

spectrometer (MRS)[9] is used to measure the down-scattered neutron spectrum between 10 and 12 MeV. (2) Neutron time of flight (nTOF) is used to measure the ratio between 3.5 and 4.5 MeV, although energies up to 6 MeV are measured currently and extension to higher energy ranges is possible.

Kinematically, DSR inferred from a specific energy range and from a particular direction samples ρL from only a specific portion of the target. If a neutron (or any particle) of mass m and with an initial energy E scatters elastically from a particle with mass M and emerges with an energy E', its angle of scattering θ is given by

$$\cos\theta = \frac{x(A+1)-(A-1)}{2\sqrt{x}}, \tag{7}$$

where $A = M/m$ and $x = E'/E$.

As a result, neutrons that scatter close to their original energies are deflected by small angles, whereas neutrons that emerge at low energies are nearly backscattered. When viewed from a single direction, the energy ranges of the neutron spectrum can be mapped to different parts of the target. The open squares in Fig. 150.57 show the locations of the MRS and nTOF detectors in the OMEGA target chamber. The contours represent 1-MeV energy ranges over the regions in the detector's view under the assumption of a point neutron source from the center for scattering from deuterons [Figs. 150.57(a) and 150.57(c)] and tritons [Figs. 150.57(b) and 150.57(d)]. An extended source would blur the regions and extend the region

somewhat but not significantly enough to change the conclusions. The 10- to 12-MeV range viewed by this detector has the advantage of focusing in on a narrower region of the target; however, a large number of detectors viewing this range would be necessary to get full, 4π sampling coverage as a result. Since multiple detectors for the higher energy range can be expensive, multiple views at lower energies (i.e., through time-of-flight measurements), which can map broader regions of the target, are considered here.
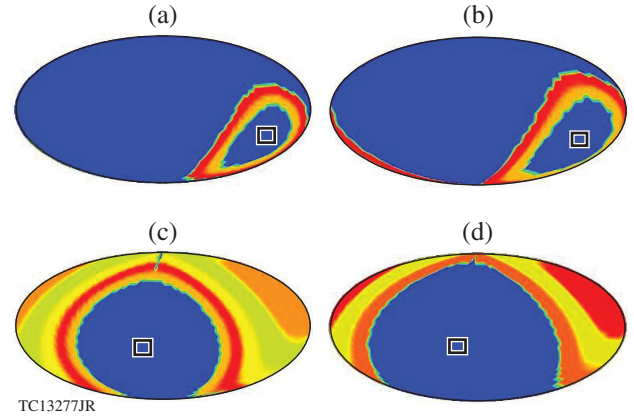

TC13277JR

Figure 150.57

(a) Projection of directions sampled by the magnetic recoil spectrometer (MRS) detector viewing deuteron elastic scattering in the 10- to 12-MeV range. The location of the detector in the OMEGA target chamber is shown as an open square. The contours represent the set of directions in which a primary DT neutron could be traveling under the assumption of a point-neutron source, which might result in it scattering from a deuteron in the direction of the detector. The ring is further broken up into 1-MeV-wide sub-rings, so that the outer sub-ring represents the area sampled by the 10- to 11-MeV region, and the inner sub-ring represents the area sampled by the 11- to 12-MeV energy range. (b) Same as (a) but for triton elastic scattering. [(c),(d)] Same as (a) and (b) but for a time-of-flight detector viewing the 1- to 6-MeV range. This range is now broken up into five 1-MeV sub-ranges. The locations of the time-of-flight detectors are shown as open squares.

For an nTOF detector using a range of 1 to 6 MeV, a much larger portion of the target can be sampled [Figs. 150.57(c) and 150.57(d)]. Note that only the higher three sub-rings are visible for triton backscatter [Fig. 150.57(d)] since the backscattered peaks for triton scattering occur around 3.5 MeV. Breaking up this observed spectrum into smaller sub-ranges makes it possible for a detector to sample ρL in smaller, narrower regions of the target. In addition, by using multiple detectors, not only ρL but also asymmetry in ρL can be mapped to different regions of the target. As discussed in the next section, however, backgrounds can significantly influence the spectrum at these lower energies and must be accounted for carefully.
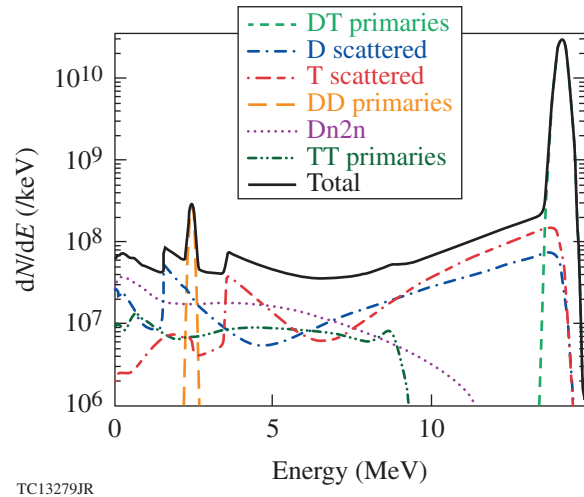
Backgrounds for Areal-Density Inference

The spectrum shown in Fig. 150.56 includes the primary and the elastically scattered neutrons. Additional effects such as thermal and Doppler broadening and multiple scattering are discussed in this section.

Multiple scattering is taken into account in the particle tracking code by recursively scattering neutrons off the background fuel ions until the effect is no longer numerically significant. Figure 150.58 demonstrates the effect that multiple scattering can have on down-scattered spectra for two different areal densities. Because DSR is approximately proportional to ρL, as we have seen, multiple scattering levels should be proportional to some power of ρL. Consequently, the effect of multiple scattering should become more significant as ρL increases. This is shown in Fig. 150.58, where for two ice-block profiles with different areal densities, the neutron spectrum is calculated with and without multiple scattering. For the higher areal density, characteristic of cryogenic implosions at the National Ignition Facility (NIF), significant differences are observed in the neutron spectra at lower energies, indicating that multiple scattering is important under such conditions. For OMEGA-scale implosions, areal densities are typically around 0.15 to 0.25 g/cm^2. In this situation, the effect of multiple scattering is negligible and can be ignored in the calculations.

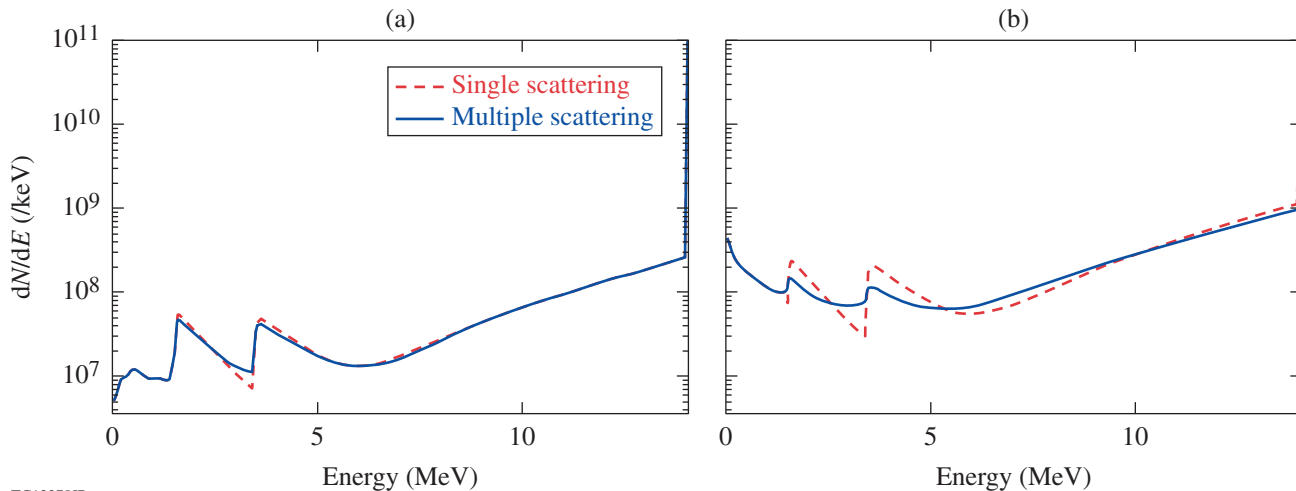All dominant components of the neutron spectrum from a cryogenic DT capsule are shown in Fig. 150.59. Again, the ice-block spectrum in Fig. 150.55 is used to calculate the spectrum. Two additional primary neutron–generating reactions are likely to occur in a DT-filled capsule: d(d,n)^{3}He and t(t,2n)^{4}He. DD primary neutrons, generated around 2.45 MeV, are not a significant background to the down-scattered neutrons since they are clearly recognizable in the spectrum. They can interact, however, with the cold fuel, for example, by elastic scattering, causing them to contribute to the background below 2.45 MeV—e.g., around the deuteron backscattered peak.

TC13279JR

Figure 150.59
Neutron spectra generated by *IRIS3D* including background reactions along with thermal broadening, Doppler broadening, and multiple scattering.

TC13278JR

Figure 150.58
Spectra generated by *IRIS3D* considering only DT primaries and deuteron and triton scattering, with and without multiple scattering: (a) for the ice-block profile shown in Fig. 150.56, which has a ρR of 0.32 g/cm^2; and (b) for the same profile, but with a higher shell density of 500 g/cm^3, resulting in a ρR of 1.52 g/cm^2.

Primary neutrons from the T–T reaction, on the other hand, do produce neutrons that act as background to the down-scattered signal because the T–T reaction produces three products, so the energies of the outgoing neutrons can be anywhere from 0 up to almost 10 MeV. Unlike the down-scattered spectrum, however, T–T reactions are independent of ρL. Since *IRIS3D* also assumes that the reaction is isotropic (detailed cross-section information is unavailable), this background is assumed to be independent of the viewing angle.

Neutrons produced from the deuteron breakup reaction, d(n,2n)p, are yet another source of background to the down-scattered spectrum. Similar to the elastic-scattering reaction, this reaction is proportional to ρL. In *IRIS3D*, this reaction is calculated only when the incoming neutron is a DT primary neutron because of the unavailability of cross sections for other energies. With an end point of 11.8 MeV, this interaction acts as a background mostly in the lower-energy portions of the spectrum. Note that when areal-density asymmetries are present, this reaction can result in ambiguities in the interpretation of areal densities from the down-scattered neutron spectrum. The directionality of neutrons from this reaction is shown in Fig. 150.60. Neutrons are launched radially from the center of the target and the locations of the product neutrons are plotted in neutrons per steradian. Figure 150.60 shows that the large

majority of deuteron-breakup neutrons emerge in the forward direction, but because there is no 1-to-1 correspondence between energy and scattering angle for an individual deuteron-breakup neutron (because there are three product particles), even these forward-emerging neutrons can have arbitrarily low outgoing energies. Therefore, an exact interpretation of the down-scattered neutron spectrum is challenging since it requires knowledge of the areal-density asymmetry to subtract the background.

The cumulative neutron spectrum (including all backgrounds) is shown in Fig. 150.61. The figure indicates that at lower energies, backgrounds can significantly influence the spectrum and therefore the inferred areal density. This is also summarized in Table 150.VI, which indicates that the ρL inferred from the calculated spectra in the 3.5- to 4.5-MeV range including the background is considerably larger than the assumed areal density, whereas the background has a marginal effect on the inferred areal density in the 10- to 12-MeV range.
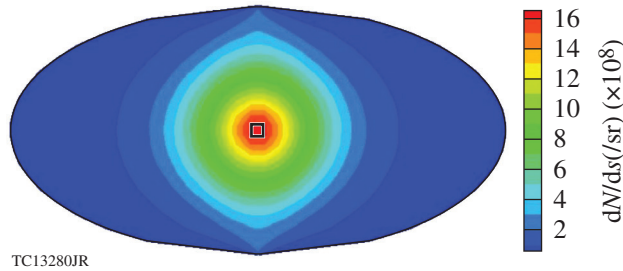

TC13280JR

Figure 150.60
Hammer projection representing angular distribution of deuteron-breakup neutrons. Each point on the surface of a projection represents a direction in the target chamber.
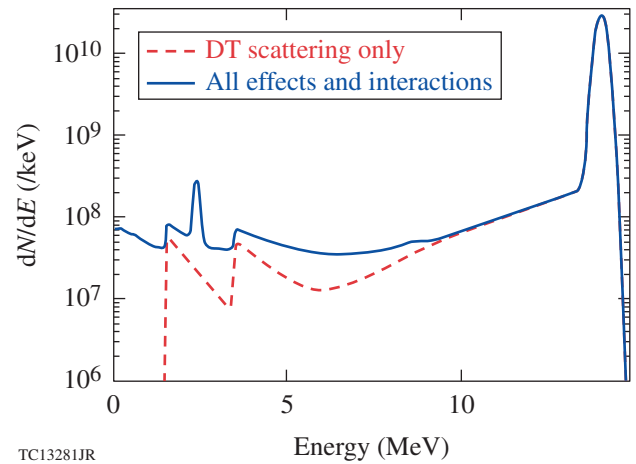

TC13281JR

Figure 150.61
Spectra generated by *IRIS3D* for the profile shown in Fig. 150.56 with and without background effects. The areal density inferred from each spectrum in the 3.5- to 4.5-MeV and 10- to 12-MeV ranges is shown in Table 150.VI.

Table 150.VI: The ρL values inferred from the spectra shown in Fig. 150.61 over the specified energy ranges. These values should be compared to a target $\rho R \sim 0.32$ g/cm^2.

Inferred ρL (g/cm^2)	3.5 to 4.5 MeV	10 to 12 MeV
DT scattering only	0.337	0.338
All effects and interactions	0.559	0.340

Detecting Areal Density and Asymmetries

Background can also have an effect on the inference of ρR asymmetries. Figure 150.62 shows how the detection of areal density around an asymmetric target can be affected by the inclusion of background for two different asymmetry patterns. Asymmetric profiles are obtained by perturbing the ice-block profiles with Legendre modes. To illustrate the effect, an $\ell = 1$ pattern with a peak-to-valley amplitude of 0.2 g/cm^2 is imposed on the profile [Fig. 150.62(a)]. In what follows, it is assumed that infinite coverage around the target chamber is available. When the 3.5- to 4.5-MeV range is used to infer areal density, the opposite phase is measured for the mode [Fig. 150.62(b)]. This is because the neutrons being observed are backscattered and originate from the opposite side of the target from the detector. The minimum and maximum inferred areal densities when the background contributions are not calculated are 0.27 and 0.41 g/cm^2, respectively, so the maximum-observable contrast is $\sim$0.14 g/cm^2—less than the imposed amplitude primarily because of the averaging of the target caused by the finite solid angle of the detectors. When background contributions are included, the $\ell = 1$ pattern is still clearly visible, but the maximum-observable contrast drops to $\sim$0.06 g/cm^2 [Fig. 150.62(c)]. Consequently, while absolute values are not inferred accurately, the overall asymmetry pattern is still encoded in the neutron spectra if the pattern is dominated by $\ell = 1$.

Somewhat different results are obtained when an $\ell = 2$ mode is imposed on the profile [Fig. 150.62(d)]. The $\ell = 2$ pattern is also apparent whether or not background contributions are considered. Additionally, the phase of the underlying areal-density pattern is reproduced by the inferred areal density [Fig. 150.62(b)]. Since the asymmetry being applied is now an even mode, sampling the rear of the target actually results in the same areal density being sampled as would be seen at the front of the target, when viewed from any particular direction. The maximum-observable contrast is $\sim$0.080 g/cm^2; when all background contributions are considered, this number drops to only $\sim$0.075 g/cm^2. The inclusion of background does not significantly hinder asymmetry detection for this mode, relative to the $\ell = 1$ perturbation. This is again because of the opposite parities of the $\ell = 1$ and $\ell = 2$ modes. Recall from **Backgrounds for Areal-Density Inference** (p. 104) that (1) the deuteron-breakup background is ρR dependent; (2) its neutrons emerge mostly in the forward direction (see Fig. 150.60); and (3) it is most significant in the backscattered (low-energy) portion of the neutron spectra, including the 3.5- to 4.5-MeV range. Therefore, when a detector infers ρL using this range, it samples ρL simultaneously from the opposite side of the target via elastically backscattered neutrons and the front side of the target via deuteron-breakup neutrons. In odd-mode asymmetries, these two locations will always have opposite areal densities, hindering the detection of those asymmetries, while for even-
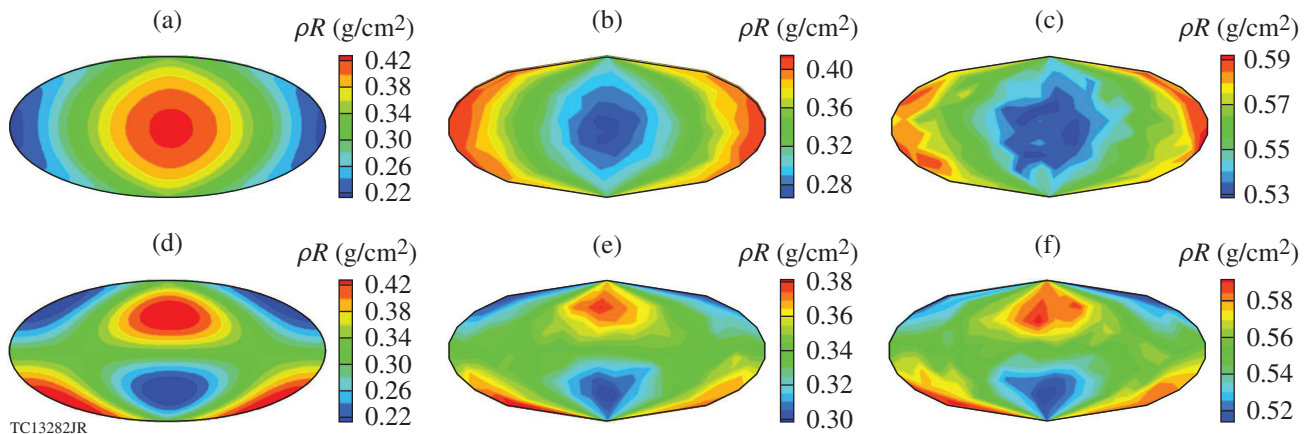

TC13282JR

Figure 150.62

(a) Hammer plot of the line integral of ρR from the center of the target for a profile with an imposed $\ell = 1$ mode. As in Fig. 150.57, each point represents a location in the target chamber. The profile used is the same as that shown in Fig. 150.56, but with the spherical-harmonic perturbation applied to the value of the density in each cell based on its location. (b) Hammer plot of observed ρL for the profile shown in (a). At each point is plotted the ρL inferred from a detector at that location looking at the 3.5- to 4.5-MeV range, as calculated by *IRIS3D*, considering only DT primaries and single deuteron and triton scattering. (c) Same as (b), but with all effects and interaction calculated; [(d)–(f)] same as (a)–(c), but an $\ell = 2$ mode imposed on the ice-block profile.

mode asymmetries, they will always have equal areal densities, enhancing the detection of the asymmetries. Also note that the contrast is reduced relative to the 0.2-g/cm^2 amplitude of the imposed mode. This is caused by the shorter wavelength of the asymmetry and the finite solid angle of the detector.

The decreasing contrast with increasing mode number is demonstrated in Fig. 160.63. Even with infinite coverage and background ignored, the contrast for an imposed mode with $\ell = 4$ falls to 8% of the imposed value for the backscattered neutrons (3.5 to 4.5 MeV) and to 17% for the forward-scattered neutrons (10 to 12 MeV)—extremely low values that likely cannot be detected, indicating that the limit in diagnosing asymmetries is likely longer than the wavelengths corresponding to $\ell = 4$.

Background subtraction is the subject of active investigation for low-energy neutron spectra[11] and is not discussed further

(a)

ρR (g/cm^2)

0.44
0.36
0.28
0.20

(b)

ρR (g/cm^2)

0.34

0.33

(c)

ρR (g/cm^2)
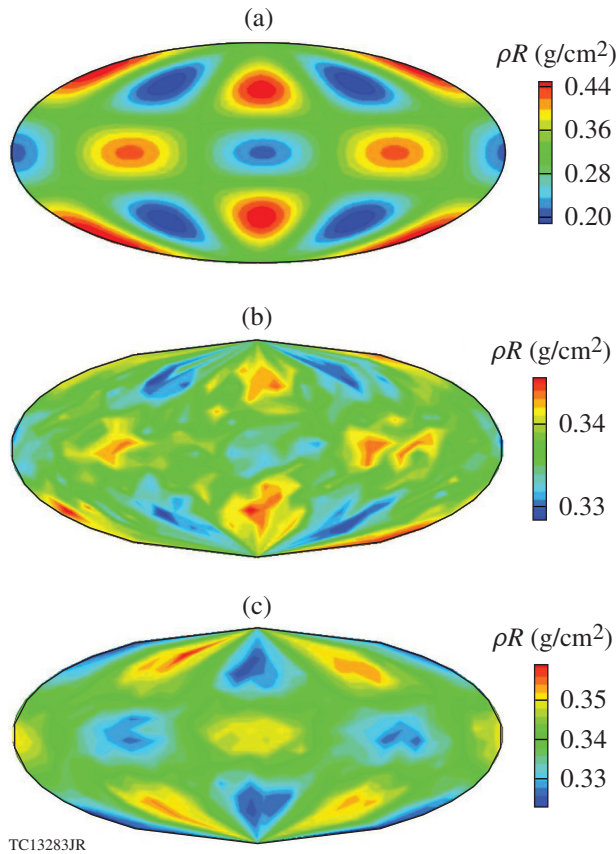
0.35
0.34
0.33

TC13283JR

Figure 150.63
(a) Same as Fig. 150.61(a), with a Legendre model $\ell = 4$ imposed on the profile; (b) same as Fig. 150.61(b), but for the profile shown in part (a) of this figure; (c) same as (b), but using the 10- to 12-MeV energy range.

in this work. For the remainder of this article, it is assumed that background can be accounted for by fitting an extended spectrum, potentially up to 10 MeV. The discussion that follows considers theoretical limits on inferred areal densities with a more realistic scenario: a finite number of detectors.

An areal-density map can be reconstructed as follows: For each detector and each energy sub-range, a ρL can be inferred based on the spectral height in that sub-range as measured by that detector, as is described in **Areal Density and Elastic Scattering** (p. 101) [see Eq. (6)]. This inferred ρL can be projected in a ring on a sphere enclosing the target as shown in Fig. 150.57. As a way to combine deuteron and triton elastic scattering, an average value of $A = 2.5$ can be used when calculating projection angles via Eq. (7). After this is done for each detector and energy sub-range, rings that overlap can be averaged together in the regions of overlap, resulting in a reconstructed areal-density map in 4π. Note that this projection assumes that neutrons are produced as a central source that introduces an error in the maps. This error is potentially quantifiable with neutron images that indicate the location of the primary source in the compressed core. Neutron imaging is not possible on OMEGA, however, because of limited neutron statistics; although, as shown below, if the perturbation were of a significantly large wavelength, the inference of areal-density variations would remain robust.

A proof-of-principle test of the reconstruction technique for ρR was performed by post-processing a 3-D *HYDRA*[4] OMEGA cryogenic implosion simulation, including realistic nonuniformity seeds from laser beam imbalances and the offset of the target in the target chamber. Primary D–T neutrons and elastically scattered neutrons were tracked for 20 time slices around peak neutron production. The density profile at peak neutron production shows a dominant $\ell = 1$ Legendre mode in the compressed core, primarily because the target was not placed at the target chamber center (Fig. 150.64). The lineout of the areal density taken from the location of the peak neutron production is also shown in Fig. 150.64(b). With infinite coverage, the inferred areal densities from the neutron spectrum are shown in Fig. 150.65(a). Since the dominant mode is given by $\ell = 1$, the phase is reversed compared to Fig. 150.64(b). Four detectors were arranged in an *ad hoc* tetrahedral fashion around the target in *IRIS3D*, and the code was used to simulate their observed spectra from 1 to 6 MeV. The locations of these detectors are shown in Fig. 150.65(b). Neutron spectra are used to reconstruct an areal-density map using the procedure described previously. The shape of the reconstructed map compares well to the lineout map seen in Fig. 150.64(b), although the contrast

(a)

(b)
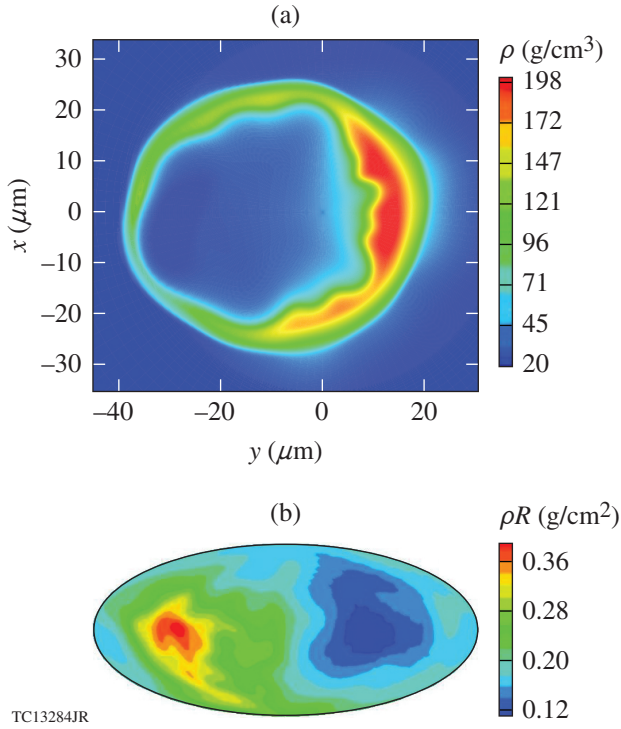
Figure 150.64
(a) Equatorial density cross section of a profile generated by *HYDRA*. An ℓ = 1 mode is apparent. (b) Hammer plot of lineout ρR of the profile shown in (a), as in Fig. 150.61(a). The ℓ = 1 mode is again the dominant feature.
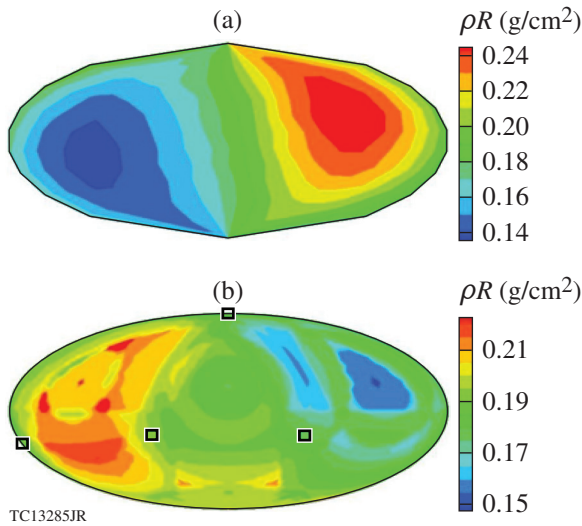

Figure 150.65
(a) Hammer plot of observed ρR using the 3.5- to 4.5-MeV range for the profile shown in Fig. 150.64. Note the expected phase change compared to Fig. 150.64(b). (b) Reconstructed ρR plot using the method described above with four detectors measuring the 1- to 6-MeV neutron range. The locations of the four directors are marked with black squares. The spectrum for each detector was split into ten 1-MeV sub-ranges.

is significantly lower, at about 0.07 g/cm², compared to about 0.26 g/cm² in the lineout or ~27%. Figure 150.65(a) suggests, however, that even with arbitrarily many detectors viewing the low-energy portion of the spectrum, the maximum-observable contrast is ~0.10 g/cm². This suggests that if one can account for background, a small number of detectors have the potential to reconstruct accurate areal-density maps of low-mode asymmetries around a target. It should be noted, however, that the success of any application of this method depends greatly on where the detectors happen to be placed relative to whatever asymmetries are present. If, as complementary experiments in room-temperature plastic shell implosions suggest, there is a systematic ℓ = 1 mode (Ref. 16), the locations for the new detectors can be optimally prescribed to detect the mode for these cryogenic implosions.

Ion-Temperature Inference

The width around the primary peak in the neutron spectrum, for D–T and D–D fusion neutrons, depends on target ion temperatures and fluid flow. The variance σ_n^2 in energy for a primary spectrum[17] is

$$\sigma_n^2 = \frac{2m_n T_i E_0}{m_n + m_\alpha} + 2m_n E_0 \sigma_v^2, \tag{8}$$
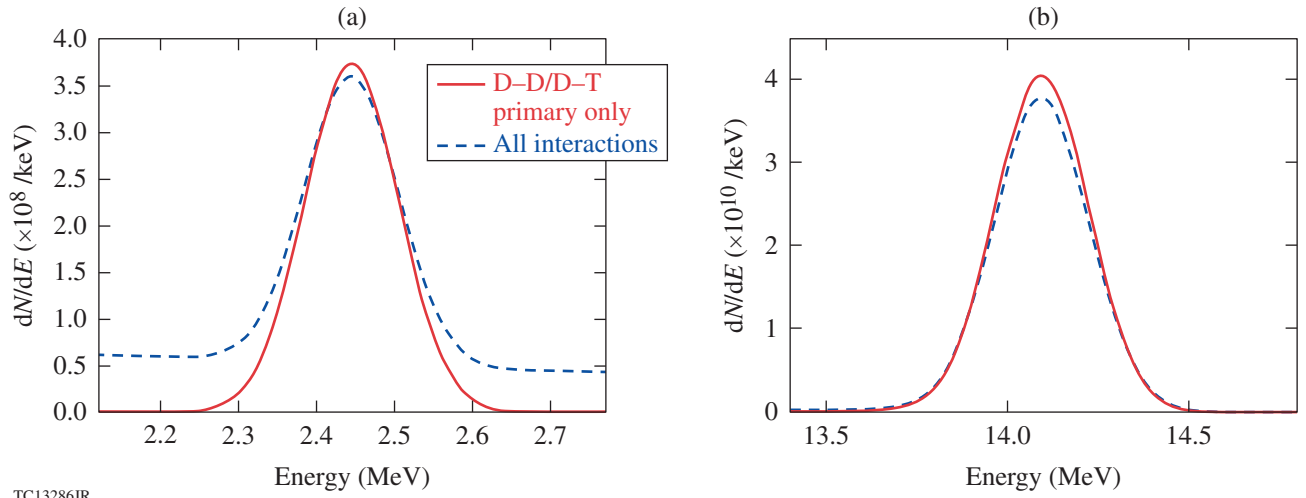
where m_n is the mass of a neutron, E_0 is the mean energy of the primary neutron (14.1 MeV for D–T primaries and 2.45 MeV for D–D primaries), m_α is the mass of the non-neutron product (^{4}He for D–T and ^{3}He for D–D), and σ_v^2 is the variance in the component of the fluid velocity along the direction of the detector; i.e.,

$$\sigma_v^2 = \mathrm{Var}\,(\vec{v}\cdot\vec{d}). \tag{9}$$

The inferred temperature from the neutron spectrum is given by[18]

$$T_{\text{fit}} = \frac{\Delta E_{\text{fit}}^2}{E_0}\frac{m_n + m_\alpha}{16 m_n \log 2}, \tag{10}$$

where ΔE_{fit} is the full width at half maximum (FWHM) of the spectrum. Therefore, the ion temperature can be inferred by measuring the primary neutron spectra. Note that effects such as fluid velocity or background contributions to the neutron spectrum, which widen D–T or D–D primary spectra, will increase the apparent D–T or D–D ion temperatures as seen from that direction (Fig. 150.66 and Table 150.VII). The neutron spectrum around the D–D fusion neutron peak [Fig. 150.66(a)]

TC13286JR

Figure 150.66

(a) Spectra, near the D–D primary peak, generated by *IRIS3D* for the profile shown in Fig. 150.56 with and without other interactions included. Note that fluid flow is not accounted for in either case. (b) Same as (a), but for the D–T primary peak. The D–T and D–D temperatures inferred from each spectrum are shown in Table 150.VII.

Table 150.VII: Ion temperature values inferred from the neutron spectra shown in Fig. 150.66 from D–D and D–T reactions. These values should be compared to a thermal temperature of 3 keV.

Inferred ion temperature (keV)	D–D reaction	D–T reaction
D–T/D–D primaries only	2.97	2.9
All neutron interactions	3.89	3.0

can be broadened because of these effects while only marginally influencing the width of the D–T fusion neutron. The two contributions to the spectra are low-energy backgrounds from other neutron processes in the target and the lowering of the height of the D–D neutron peak because of its higher scattering cross sections, which cause a significant increase in apparent ion temperature (Table 150.VII). The apparent temperature calculated from just the D–D primary spectra is 2.97 keV compared to the thermal value of 3 keV (see Fig. 150.56), while that calculated from the spectra including all contributions without any corrections to the background is 3.89 keV—a 31% increase.

These effects are relatively insignificant when inferred from the D–T neutron spectrum [Fig. 150.66(b)]. This is because (1) the scattering cross sections of 14.1-MeV neutrons are smaller compared to those of 2.45-MeV neutrons and (2) there is a lack of backgrounds above 12 MeV, including all the neutron interactions. As Table 150.VII indicates, the increase is less than 1%.

The second term in Eq. (8), corresponding to fluid flow, can significantly affect neutron spectral widths. To isolate the effect of fluid flow, the same hydrocode profile from Fig. 150.64 was used and only D–T and D–D primaries were tracked. Figure 150.67 shows that the profile contains a jet of fluid flow directed from the high-density region of the $\ell = 1$ mode to the low-density side.

The inferred ion temperatures from D–T and D–D fusion neutron spectra (Fig. 150.68) correspond closely to this flow. Observed temperatures for both D–T and D–D neutrons are highest at the positions corresponding to the extremes in density shown in Fig. 150.64(b) and lowest in a ring at about 90° to these two points. For any direction in the ring around the $\ell = 1$ mode, the jet seen in Fig. 150.67 points orthogonally to that direction, so it has a very small effect on the value of σ_v^2 as seen from that direction as calculated in Eq. (9). For the directions that point along the $\ell = 1$ mode, however, there is a large variation in $\vec{v} \cdot \vec{d}$ [Eq. (9)], leading to a large σ_n^2 [Eq. (8)]. As

a result, the apparent temperature is much higher than it would be with no fluid flow in these directions. These results indicate that with multiple views of the primary neutron spectra, the relative ion temperature values inferred can provide an indication of low-order asymmetries in the hot spot.
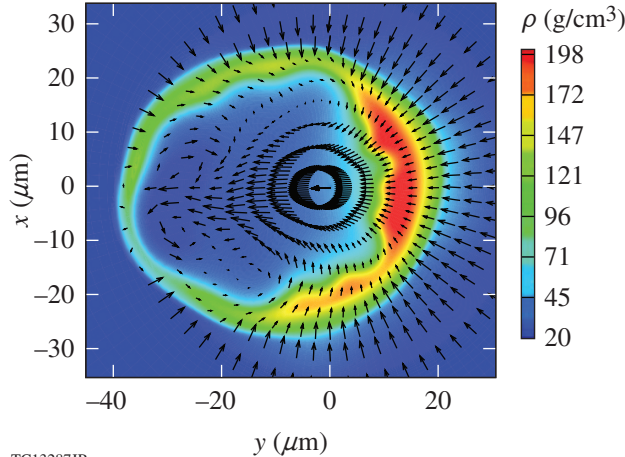

TC13287JR

Figure 150.67
Same as Fig. 150.64(a), but with additional vectors representing fluid velocity direction and magnitude.
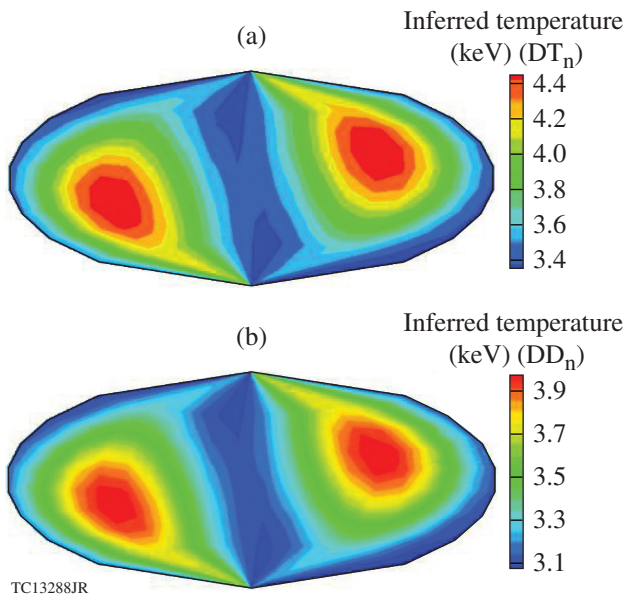

TC13288JR

Figure 150.68
(a) Hammer plot of apparent DT ion temperatures around the target for the profile shown at peak neutron production in Fig. 150.64, as calculated by *IRIS3D* considering DT neutrons only. As in previous figures, each point represents a direction in the target chamber, and the value at each point is the apparent temperature as measured from that direction. (b) Same as (a), but for apparent DD ion temperatures.

Conclusions

Using a newly developed particle tracking code *IRIS3D* (see **Appendix**, below), neutron-based spectra are used to study signatures of asymmetry in OMEGA-scale cryogenic implosions. These include areal-density variations and neutron spectral-width variations around the compressed target. Background subtraction from observed neutron spectra is extremely important for the lower-energy range (1 to 6 MeV) to infer true areal densities. It is found that because of the finite area of the target viewed by detectors, a limited number of detectors that use a neutron spectrum up to 6 MeV can provide information on the underlying asymmetric structure of the compressed shell. Although not presented in this work, it has been found that the shape of the neutron spectrum changes from the spherically symmetric shape. This information will be used to isolate the effect of asymmetry and backgrounds in future work. Background subtraction from the lower-energy D–D fusion neutron peak is critical for reliably inferring neutron width. It is also shown that measurements of neutron width can be correlated with an overall direction of fluid flow from both DD and DT ion temperatures, provided background correction has been performed for the DD temperature. Detailed simulations and comparisons with experiment for a range of implosion parameters will be presented elsewhere. We will continue to use *IRIS3D* as a postprocessor for 3-D hydrodynamic codes and will pursue detailed comparisons with observations for OMEGA cryogenic implosions.

Appendix: Structure and Methods of *IRIS3D*

IRIS3D is a parallel Monte Carlo–based neutron-tracking code with variable particle weights. Neutrons generated by a variety of interactions are tracked through a spherical grid made up of hexahedral cells such as those shown in Fig. 150.69. Note that in Fig. 150.69 and throughout this appendix, r, θ, and ϕ refer to spherical coordinates with θ denoting the polar angle and ϕ denoting the azimuthal angle. Each cell is indexed as described in the figure and is characterized by a DT fuel density, an ion temperature, and a fluid vector velocity. To preserve the hexahedral structure of each cell, *IRIS3D* imposes exclusion zones within a small distance of the origin and within a small angle of each pole that are not occupied by cells. Therefore, each vertex with an i-index of zero is not at $r =$

0 but at a very small distance from the origin, and each vertex with a j-index of zero or the maximum index is not at $\theta = 0$ or π, respectively, but at 0 plus a small angle and π minus a small angle, respectively. These exclusion zones are small enough that a very limited number of particles can pass through them in a given simulation. They have an insignificant effect on results, and particles that do pass through them are simply propagated across them by a reflection, where they continue on through the remainder of the grid as usual.
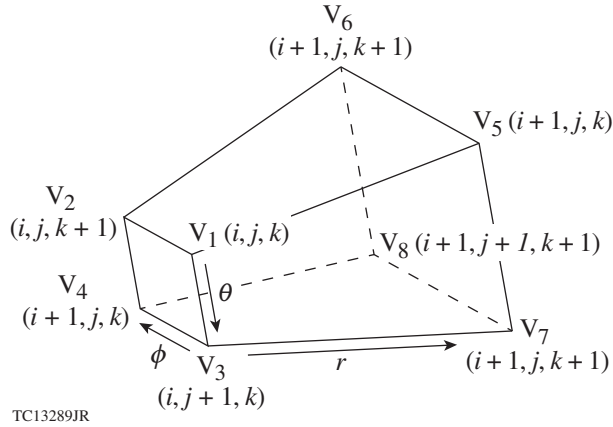

V_6
(i + 1, j, k + 1)

V_5 (i + 1, j, k)

V_2
(i, j, k + 1)

V_1 (i, j, k)

V_8 (i + 1, j + 1, k + 1)

V_4
(i + 1, j, k)

θ

φ

V_3
(i, j + 1, k)

r

V_7
(i + 1, j, k + 1)

TC13289JR

Figure 150.69
Layout of a generic hexahedral cell in *IRIS3D*. Each vertex (V) is represented by indices i, j, and k, which increase with r, θ, and ϕ, respectively, and each cell is bounded by eight vertices as shown.

IRIS3D currently models six neutron-emitting interactions. Spectra from these interactions are shown in Fig. 150.59: primary neutron–producing fusion reactions including d(t,n)^{4}He, d(d,n)^{3}He, and t(t,2n)^{4}He; and three secondary interactions including d(n,n′)d′, t(n,n′)t′, and d(n,2n)p. The secondary interactions involve the interactions of primaries as they traverse the grid.

A trajectory in *IRIS3D* is generated in some cell, (i, j, k), representing some number of neutrons y_n, all at some energy E, and moving in some direction $\vec{d} = (u, v, w)$, where $\vec{d}$ is a unit vector and u, v, and w are the direction cosines. The initial position of the trajectory, $P_0 = (x, y, z)$, is set as the centroid of the cell in which it is generated. The trajectory is tracked in a straight line through the grid.

For each cell the trajectory enters, the following process is carried out: first, initial points Q and normal vectors for the six planes of the cell are calculated; next, for each plane, the following calculation is performed:

$$\Delta s = \frac{\overrightarrow{PQ} \cdot \vec{n}}{\vec{d} \cdot \vec{n}}, \tag{11}$$

where P denotes the initial position of the trajectory within the cell and Δs represents the (possibly negative) distance the trajectory must travel along its direction to intersect with that plane. The plane that yields the smallest positive value of Δs is the next plane with which the trajectory will intersect, so it corresponds to the face of the cell through which the trajectory will exit. Next, any secondary neutron interactions the user has specified to be considered are calculated based on the physical parameters of the cell and the neutrons represented by the trajectory along with the value of Δs corresponding to the chosen plane. Finally, the trajectory's position P is changed to the position of intersection with that face and then propagated a small distance along direction d determined by convergence studies, and the particle's current cell index (i, j, k) is updated based on the face through which it exited. For example, if the particle started in cell (i, j, k) and exited through the face lying in the plane $V_1 V_2 V_3$, its new cell index would be (i, j, k), as is apparent from Fig. 150.69. If, at this point, the cell indices indicate that the trajectory has entered an exclusion zone, as described above, the particle is appropriately reflected to continue along the grid. For each trajectory, this process is carried out until the particle exits the grid. When this occurs, the trajectory is binned. Note that the target is assumed to be very small compared to the target chamber; therefore, the target is assumed to be essentially point-like from the view of any detectors, so trajectories are binned only according to their direction $\vec{d}$.

IRIS3D accounts for two different types of detectors that bin trajectories. First, a grid of detectors is placed around the target. The grid lines are at constant θ or ϕ values, so for each trajectory, its (θ, ϕ) direction is calculated according to d, and it is binned in whichever grid rectangle its (θ, ϕ) direction lies. In addition, detectors at specific (θ, ϕ) locations and with specific solid angles Ω are specified by the user (for example, these would correspond to existing detector locations on OMEGA). For each of these detectors, a trajectory is binned in them if and only if

$$\vec{d} \cdot \vec{l} \geq 1 - \frac{\Omega}{2\pi}, \tag{12}$$

where $\vec{l}$ is a unit vector in the direction of the detector. Detectors collect both time-integrated and time-resolved neutron spectra.

In what follows, we discuss in detail how trajectories are launched. First, the number of fusion reactions in each cell is calculated. To do this, a reactivity $\langle \sigma v \rangle$ is calculated in each

cell based on cell ion temperatures using the analytic fit given in Ref. 19, and then the number of fusion reactions, y_{cell}, is calculated as

$$y_{cell} = \frac{n_i n_j}{1 + \delta_{ij}} \langle \sigma v \rangle_{ij} V \Delta t$$

$$= \frac{f_i f_j}{1 + \delta_{ij}} \left(\frac{\rho}{m}\right)^2 \langle \sigma v \rangle_{ij} V \Delta t, \tag{13}$$

where n_i and n_j are ion densities for the two different ions, f_i and f_j are the ion fractions for the two ions characterized during the target-fabrication process, V is the cell volume, Δt is the duration of the time slice being processed for neutron spectra, and δ_{ij} is the Kronecker delta (= 1 if $i = j$, i.e., for D–D fusion). If N is the total number of trajectories that are to be launched across the entire grid for that time step (determined by requiring adequate statistics in the calculated spectra), then the number of trajectories launched per cell is $\left(y_{cell} / \sum y_{cell}\right) \cdot N$.

For each primary trajectory to be launched from a cell centroid, d is chosen as a random unit vector (since the primary reactions considered in this work are isotropic) and E sampled from a normal distribution with mean μ and standard deviation σ determined by[17]

$$\mu = E_0 + (\vec{v} \cdot \vec{d}) \sqrt{2 m_n E_0} \tag{14}$$

and

$$\sigma = \sqrt{\frac{2 m_n T_i E_0}{m_n + m_\alpha}}, \tag{15}$$

where, for example, $E_0 = 14.1$ MeV is the mean neutron energy from the D–T fusion reaction; $\vec{v}$ the cell fluid velocity; m_n and m_α are the masses of the neutron and alpha particles, respectively; and T_i is the cell ion temperature. The second term in the expression for the mean of the energy distribution takes into account Doppler shifts in the energy of the neutron caused by the fluid velocity. The expression for the standard deviation takes into account the broadening of the neutron spectrum caused by the plasma temperature.[18]

T–T reactions are treated similarly. Reactivity for temperatures below 1 keV is calculated using the analytic fit given in Ref. 20, while reactivity for ion temperatures above or equal to 1 keV is calculated by linear interpolation using the look-up table given in Ref. 21. The initial neutron energy E_0 is sampled

from a distribution obtained by an R-matrix calculation,[22] which agrees well with experimental measurements.[22] Note that the T–T primary neutrons are not launched in pairs that obey the conservation laws but instead are launched one at a time, independently. Momentum and energy are conserved only with adequate statistics.

Secondary reactions are considered next. *IRIS3D* starts by estimating a value of y', the total number of deuteron-scattered neutrons:

$$y' = y_{total} \frac{f_D \sigma_{14.1}}{m} \rho R, \tag{16}$$

where y_{total} is the total number of primary neutrons generated $\left(= \sum y_{cell}\right)$, $\sigma_{14.1}$ is the cross section for deuteron elastic scattering for neutrons at 14.1 MeV, and ρR is a directionally averaged lineout of the areal density. For multiple scattering, where energies other than 14.1 MeV can contribute to the spectrum, the scattering cross section is obtained from an energy-dependent look-up table given by Ref. 23. The number N_s of secondary trajectories launched from a given interaction location is a code input to obtain converged results; therefore the weight of each trajectory is $y_0 = y'_{total} / N_s$.

The number of deuteron (or triton)-scattering interactions, y', is calculated as

$$y' = y \frac{f_{D/T} \sigma_{D/T}}{m} \rho \Delta s, \tag{17}$$

where y is the number of neutrons represented by the trajectory, σ is the cross section for deuteron elastic scattering for neutrons with energy E, and Δs is the path length. At this point, y is replaced with $y - y'$ since the primary trajectory loses any neutrons that scatter away. The weight of the trajectory is y_0, and a scattering angle θ is sampled by interpolating between a set of energy-dependent angular cross sections from Ref. 15. An azimuthal scattering angle ϕ is then picked randomly over the interval $(0, 2\pi)$, and the scattered neutron trajectory direction $\vec{d}'$ is set as

$$\vec{d}' = \vec{a} \sin\theta \cos\phi + \vec{b} \sin\theta \sin\phi + \vec{d} \cos\theta, \tag{18}$$

where $\vec{d}$ is the direction of the original trajectory and $\vec{a}$ and $\vec{b}$ are a set of unit vectors that are orthogonal to each other and to $\vec{d}$. Finally, E', the energy of the scattered neutrons, is determined based on θ using Eq. (7). Once generated, the scattered trajectory is again handled as described previously.

The deuteron-breakup interaction is modeled somewhat differently. A look-up table for angular distributions of emerging particles is available only for 14.1-MeV incident neutrons, so the interaction is considered only in the case where the original trajectory represents D–T primary neutrons. A constant value of $\sigma = \sigma_{14.1} = 164.821$ mb is used for both Eqs. (16) and (17) (see Ref. 24). Two trajectories are launched for the product neutrons since two neutrons are produced in each break-up reaction. Since there is no deterministic relationship between the angle and energy of each emergent neutron, the scattering angle is sampled from a distribution calculated based on Ref. 25, and energy is sampled from a distribution based on that scattering angle. As was the case with the T–T primary reaction, the neutrons' energies and scattering angles are both sampled independently, so momentum and energy are not necessarily conserved in any particular interaction but conservation improves with increasingly better statistics.

If a series of time slices from the same implosion are used instead, the process is repeated for each time step and the results are accumulated over time.

REFERENCES

1. J. Nuckolls *et al*., Nature **239**, 139 (1972).

2. T. R. Boehly, D. L. Brown, R. S. Craxton, R. L. Keck, J. P. Knauer, J. H. Kelly, T. J. Kessler, S. A. Kumpan, S. J. Loucks, S. A. Letzring, F. J. Marshall, R. L. McCrory, S. F. B. Morse, W. Seka, J. M. Soures, and C. P. Verdon, Opt. Commun. **133**, 495 (1997).

3. J. Delettrez, R. Epstein, M. C. Richardson, P. A. Jaanimagi, and B. L. Henke, Phys. Rev. A **36**, 3926 (1987).

4. M. M. Marinak *et al*., Phys. Plasmas **8**, 2275 (2001).

5. Lord Rayleigh, Proc. London Math Soc. **XIV**, 170 (1883); G. Taylor, Proc. R. Soc. London Ser. A **201**, 192 (1950); R. Kishony and D. Shvarts, Phys. Plasmas **8**, 4925 (2001).

6. C. Stoeckl, R. Epstein, R. Betti, W. Bittle, J. A. Delettrez, C. J. Forrest, V. Yu. Glebov, V. N. Goncharov, D. R. Harding, I. V. Igumenshchev, D. W. Jacobs-Perkins, R. T. Janezic, J. H. Kelly, T. Z. Kosc, R. L. McCrory, D. T. Michel, C. Mileham, P. W. McKenty, F. J. Marshall, S. F. B. Morse, S. P. Regan, P. B. Radha, B. S. Rice, T. C. Sangster, M. J. Shoup III, W. T. Shmayda, C. Sorce, W. Theobald, J. Ulreich, M. D. Wittman, D. D. Meyerhofer, J. A. Frenje, M. Gatu Johnson, and R. D. Petrasso, Phys. Plasmas **24**, 056304 (2017).

7. F. J. Marshall, V. N. Goncharov, V. Yu. Glebov, B. Peng, S. P. Regan, T. C. Sangster, and C. Stoeckl, "A Framed, 16-Image Kirkpatrick–Baez X-Ray Microscope," submitted to Review of Scientific Instruments.

8. R. Betti, P. Y. Chang, B. K. Spears, K. S. Anderson, J. Edwards, M. Fatenejad, J. D. Lindl, R. L. McCrory, R. Nora, and D. Shvarts, Phys. Plasmas **17**, 058102 (2010).

9. D. C. Wilson et al., Nucl. Instrum. Methods Phys. Res. A **488**, 400 (2002).

10. J. A. Frenje, D. T. Casey, C. K. Li, J. R. Rygg, F. H. Séguin, R. D. Petrasso, V. Yu. Glebov, D. D. Meyerhofer, T. C. Sangster, S. Hatchett, S. Haan, C. Cerjan, O. Landen, M. Moran, P. Song, D. C. Wilson, and R. J. Leeper, Rev. Sci. Instrum. **79**, 10E502 (2008).

11. C. J. Forrest, P. B. Radha, V. Yu. Glebov, V. N. Goncharov, J. P. Knauer, A. Pruyne, M. Romanofsky, T. C. Sangster, M. J. Shoup III, C. Stoeckl, D. T. Casey, M. Gatu-Johnson, and S. Gardner, Rev. Sci. Instrum. **83**, 10D919 (2012).

12. T. J. Murphy, Phys. Plasmas **21**, 072701 (2014).

13. ENDF/B-N1.1, IAEA Nuclear Data Services.

14. S. Skupsky and S. Kacenjar, J. Appl. Phys. **52**, 2608 (1981).

15. J. A. Frenje, C. K. Li, F. H. Séguin, D. T. Casey, R. D. Petrasso, D. P. McNabb, P. Navratil, S. Quaglioni, T. C. Sangster, V. Yu. Glebov, and D. D. Meyerhofer, Phys. Rev. Lett. **107**, 122502 (2011).

16. C. K. Li, F. H. Séguin, D. G. Hicks, J. A. Frenje, K. M. Green, S. Kurebayashi, R. D. Petrasso, D. D. Meyerhofer, J. M. Soures, V. Yu. Glebov, R. L. Keck, P. B. Radha, S. Roberts, W. Seka, S. Skupsky, C. Stoeckl, and T. C. Sangster, Phys. Plasmas **8**, 4902 (2001).

17. V. N. Goncharov, T. C. Sangster, R. Betti, T. R. Boehly, M. J. Bonino, T. J. B. Collins, R. S. Craxton, J. A. Delettrez, D. H. Edgell, R. Epstein, R. K. Follet, C. J. Forrest, D. H. Froula, V. Yu. Glebov, D. R. Harding, R. J. Henchen, S. X. Hu, I. V. Igumenshchev, R. Janezic, J. H. Kelly, T. J. Kessler, T. Z. Kosc, S. J. Loucks, J. A. Marozas, F. J. Marshall, A. V. Maximov, R. L. McCrory, P. W. McKenty, D. D. Meyerhofer, D. T. Michel, J. F. Myatt, R. Nora, P. B. Radha, S. P. Regan, W. Seka, W. T. Shmayda, R. W. Short, A. Shvydky, S. Skupsky, C. Stoeckl, B. Yaakobi, J. A. Frenje, M. Gatu-Johnson, R. D. Petrasso, and D. T. Casey, Phys. Plasmas **21**, 056315 (2014).

18. H. Brysk, Plasma Phys. **15**, 611 (1973).

19. H. S. Bosch and G. M. Hale, Nucl. Fusion **32**, 611 (1992); **33**, 1919(E) (1993).

20. A. Peres, J. Appl. Phys. **50**, 5569 (1979).

21. J. R. McNally, Jr., K. E. Rothe, and R. D. Sharp, Oak Ridge National Laboratory, Oak Ridge, TN, Report ORNL/TM-6914 (1979).

22. D. B. Sayre, C. R. Brune, J. A. Caggiano, V. Y. Glebov, R. Hatarik, A. D. Bacher, D. L. Bleuel, D. T. Casey, C. J. Cerjan, M. J. Eckart, R. J. Fortner, J. A. Frenje, S. Friedrich, M. Gatu-Johnson, G. P. Grim, C. Hagmann, J. P. Knauer, J. L. Kline, D. P. McNabb, J. M. McNaney, J. M. Mintz, M. J. Moran, A. Nikroo, T. Phillips, J. E. Pino, B. A. Remington, D. P. Rowley, D. H. Schneider, V. A. Smalyuk, W. Stoeffl, R. E. Tipton, S. V. Weber, and C. B. Yeamans, Phys. Rev. Lett. **111**, 052501 (2013).

23. R. C. Shah, B. M. Haines, F. J. Wysocki, J. F. Benage, J. A. Fooks, V. Glebov, P. Hakel, M. Hoppe, I. V. Igumenshchev, G. Kagan, R. C. Mancini, F. J. Marshall, D. T. Michel, T. J. Murphy, M. E. Schoff, K. Silverstein, C. Stoeckl, and B. Yaakobi, Phys. Rev. Lett. **118**, 135001 (2017).

24. P. G. Young, G. M. Hale, and M. G. Chadwick, ENDF/B-VII.1, IAEA Nuclear Data Services, 22 December 2011.

25. A. Deltuva, Institute of Theoretical Physics and Astronomy, Vilinus University, Vilinus, Lithuania, private communication (2016).